Synthesis of phase pure iron oxide polymorphs thin films and their enhanced magnetic properties

Pawan Kumar · Heung No-Lee · Rajesh Kumar

Abstract The α-Fe_2O_3 thin film was prepared on liquid–vapor interface at room temperature by a facile and cost effective method, which was converted to Fe_3O_4 and γ-Fe_2O_3 films by reduction and oxidation process. The morphological and structural characterizations reveal the average crystallites size in α-Fe_2O_3, Fe_3O_4 and γ-Fe_2O_3 films 12.8, 9.2 and 19 nm with rms roughness 4.35, 4.60 and 8.21 nm, respectively. From magnetic measurements, the α-Fe_2O_3 thin film shows a room temperature superparamagnetic behavior with saturation magnetization 18 emu/cm^3, while Fe_3O_4 and γ-Fe_2O_3 thin films exhibit ferrimagnetic behavior with saturation magnetization values 414.5 and 148 emu/cm^3, respectively. A significantly higher value of saturation magnetization is observed in α-Fe_2O_3 film, which is trusted due to the uncompensated surface spins in the film. The converted Fe_3O_4 film also shows enhanced saturation magnetization due to the reduction in antiphase boundaries, whereas the magnetization in γ-Fe_2O_3 film decreases comparatively. The magnetic property of the γ-Fe_2O_3 is explained on the basis of the Fe^{3+} ions vacancy at the octahedral position in its structure.

1 Introduction

Among various magnetic materials, the iron oxides represent an important class of transition-metal oxide magnetic materials. Films made of iron oxide have attracted significant interest not only because of their fascinating physicochemical properties but also their potential use in scientific and technological applications [1–5]. It is well known that at room temperature the iron oxide exhibits three stoichiometric forms viz. magnetite (Fe_3O_4), maghemite (γ-Fe_2O_3) and hematite (α-Fe_2O_3). Among these structures the Fe_3O_4 and γ-Fe_2O_3 have spinel structure and α-Fe_2O_3 shows corundum structure [6] with iron cation in γ-Fe_2O_3 and α-Fe_2O_3 in Fe^{3+} state and in Fe_3O_4 the it exists in Fe^{3+} as well as Fe^{2+} state [7]. From technological importance, the Fe_3O_4 showing ferrimagnetic nature is highly used in electro-optical industry also due to its high Curie temperature ($T_c = 585$ °C) and 100 % spin polarization the thin films of Fe_3O_4 have wide applications in spintronics [3, 7]. Similarly, the α-Fe_2O_3 due to its optical band gap in visible region is used in hydrogen production from water photo catalysis [8], and γ-Fe_2O_3 being a ferrimagnetic material is used in high density magnetic storage [9].

Looking to the great technological applications of the iron oxide films, a facile route for their formation with highly controlled, uniform morphologies and novel properties is required. Although, many conventional vacuum techniques such as atmospheric pressure chemical vapor deposition [10], electron beam evaporation [11], pulse laser deposition [12], atomic layer deposition [13], reactive DC magnetron sputtering [14], metal organic deposition etc. [15] have been widely reported. However, the practical application of these growth techniques has been restricted because of high cost of manufacturing equipment and limitations on achieving a large surface area with uniform deposition [16, 17]. For example, while considering the solution route to form the magnetic films, it would results in agglomerated structure rather than a film due the

P. Kumar · R. Kumar (✉)
Jaypee University of Information Technology,
Waknaghat, Solan 173234, Himachal Pradesh, India
e-mail: rajesh.kumar@juit.ac.in

H. No-Lee · R. Kumar
Gwangju Institute of Science and Technology, Gwangju 500712,
Republic of Korea

presence of magnetic nanoparticles [18]. Also, the phase purity is an important issue in the formation of a film. It is quite difficult to produce iron oxide films in highly pure phase since other oxide phases are also formed during the synthesis of a particular iron oxide [19]. Therefore, for better performance of the iron oxide film based device, utilization of highly pure phase iron oxide films with controlled morphology is required.

The Fe_3O_4 and γ-Fe_2O_3 can be obtained by the reduction and oxidation processes of α-Fe_2O_3. However, there are many reports on the conversion of nanotubes and nanoparticles of α-Fe_2O_3 to Fe_3O_4 by reduction and then to γ-Fe_2O_3 by oxidation [20, 21] but there are only few reports on the conversion of thin film of α-Fe_2O_3 by the reduction and oxidation processes [22]. Also, structural and morphologies properties with phase purity of the iron oxide films is not emphasized. If the non-magnetic film α-Fe_2O_3 is taken as the starting material then the magnetic films Fe_3O_4 and γ-Fe_2O_3 can be obtained just by conversion process, while preserving the morphology of film. Here we report the preparation of α-Fe_2O_3 thin film by a very simple chemical route [23]. The formed α-Fe_2O_3 film was successfully converted to Fe_3O_4 thin film by reduction and then to γ-Fe_2O_3 film by heating in presence of O_2. These films were investigated for structural, morphological, magnetic properties and their phase purity. The prepared iron oxide films show excellent structural, morphological magnetic properties and phase purity.

2 Experimental

The α-Fe_2O_3 thin film was prepared on liquid–vapor interface using a very simple method [23]. A precursor solution with 24 mM $FeCl_2$ and 22 mM $FeCl_3 \cdot 6H_2O$ containing 64 μM of polyvinyl alcohol (PVA) was prepared initially. The solution stirred for 10 min at 80 °C was transferred immediately to a petri dish in an argon (Ar) chamber. Then a measured volume of NH_3 vapor was poured into the chamber and it was sealed for 10 min to occur the chemical reaction of NH_3 vapor with solution surface. After reaction, the liquid–vapor interface converted into a thin floating film. The film was transferred to the surface of a glass substrate annealed in air at 500 °C in a tube furnace. The as prepared α-Fe_2O_3 film was then reduced in presence of H_2 gas to obtain Fe_3O_4 film according to thermal reaction;

$$3\alpha\text{-}Fe_2O_3 + H_2 \xrightarrow{500\,°C} 2Fe_3O_4 + H_2O \qquad (1)$$
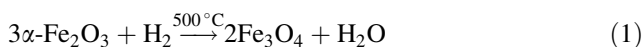
For the reduction, the α-Fe_2O_3 film was annealed at 500 °C inside a quartz tube under the flow of mixed gas (H_2:Ar = 50:100 cm^3/min) for 1 h. Here, Ar was used as
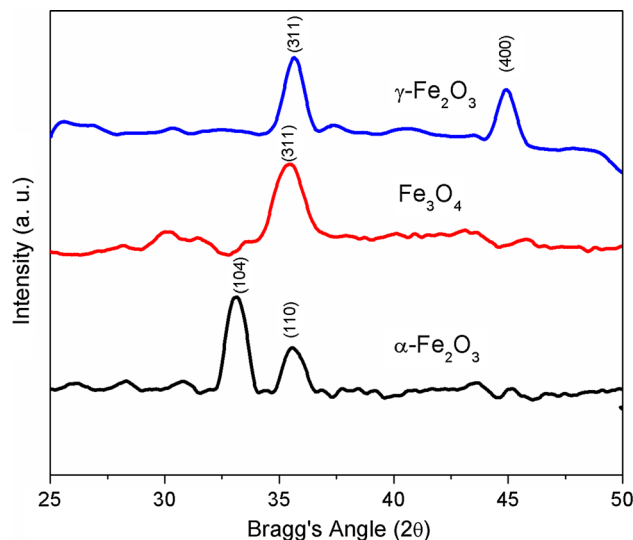
Fig. 1 XRD patterns of the iron oxide thin films

dilution and carrier gas. After 1 h of annealing, the furnace was cooled down to room temperature at the rate of 5 °C/min keeping Ar gas to flow.

Similarly, for the formation of γ-Fe_2O_3 films, the as prepared Fe_3O_4 film was oxidized in presence of O_2 gas. For the oxidation, the Fe_3O_4 film was annealed in constant flow of O_2 gas in a quartz tube at 350 °C for 2 h.

$$4Fe_3O_4 + O_2 \xrightarrow{350\,°C} 6\gamma\text{-}Fe_2O_3 \qquad (2)$$

2.1 Microstructural and magnetic characterization

For the morphological and structural properties, the prepared iron oxide films were characterized using transmission electron microscopy (TEM), atomic force microscopy (AFM) and X-ray diffraction (XRD) techniques. The phases of iron oxide thin films were analyzed by Raman spectroscopy and UV–Visible spectrophotometer, and for magnetic characterizations vibrating sample magnetometer (VSM) was used.

3 Result and discussion

The obtained typical XRD patterns for α-Fe_2O_3, Fe_3O_4 and γ-Fe_2O_3 thin films are presented in Fig. 1. All the iron oxide films are well crystalline, having matched their diffraction peaks with standard diffraction peaks. The diffraction peaks of the three iron oxide films matches with diffraction peaks of bulk α-Fe_2O_3 [Joint Committee on Powder Diffraction Standards (JCPDS card no. 89-8104)], magnetite Fe_3O_4 (JCPDS no. 89-0951) and maghemite γ-Fe_2O_3 (JCPDS no. 89-5892), respectively. The observed

Table 1 Value of 2θ, grain size (D_{hkl}), lattice spacing (d_{hkl}), lattice parameter ($a = b$, c), strain (ε_{hkl}) and dislocation density (δ) for iron oxide thin films from XRD result

Sample	2θ	D_{hkl} (nm)	d_{hkl}	$a = b$ (Å)	c (Å)	Strain (ε_{str})	Dislocation density (δ) (10^{-15})
α-Fe$_2$O$_3$	33.17	13.8	2.739	5.043	13.78	0.01027	2.13456
	35.56	11.9	1.936				
Fe$_3$O$_4$	35.47	9.2	2.527	8.383	8.383	0.01255	2.45897
γ-Fe$_2$O$_3$	35.67	16.6	2.514	8.338	8.338	0.0110	1.4169
	44.93	21.4	2.015	8.060	8.060		

broadening of the peaks in XRD indicates the presence of small crystallites. From XRD, the average crystallites size (D_{hkl}) inside the films was estimated using Scherrer's formula [24],

$$D_{hkl} = \frac{0.9\lambda}{\beta_{hkl}\cos\theta}. \qquad (3)$$

where $\lambda = 0.154$ nm corresponds to the wavelength of Cu K$_\alpha$ radiation and β_{hkl} is full width half maximum (FWHM) of the diffraction peak from (hkl) crystal planes. Using above relation, the calculated average crystallite size for α-Fe$_2$O$_3$, Fe$_3$O$_4$ and γ-Fe$_2$O$_3$ thin films is given in Table 1. We also calculated lattice spacing (d) as mentioned in Table 1, which is found in good agreement with the reported values [21]. A change in the phase while converting the α-Fe$_2$O$_3$ film to Fe$_3$O$_4$ is attributed as a shift in the XRD peak from 32.64° to 35.47° and also the absence of the (024) peak. Similarly, on oxidation the shift of XRD peak at 35.47° to higher value of 2θ and a peak at 44.93° is corresponding to the new phase i.e. γ-Fe$_2$O$_3$ (JCPDS no. 89-5892).

Owing to different surface energies along different plane or orientations [26], the properties and stability of a thin film depend upon the degree of preferred orientation [25]. Therefore, the study of preferred orientation factor is needed. The magnitude of preferred orientation factor (f) for a given plane i.e. XRD peak can be calculated relative to other planes [27]. The preferred orientation factor e.g. for (104) plane is denoted as f(104) and can be calculated by evaluating the fraction of intensity of the (104) plane over the sum of intensities of all peaks within a given 2θ range [27]. Using this method, the preferred orientation factors for α-Fe$_2$O$_3$ thin film was calculated which is f(104) = 0.782. Similarly, for Fe$_3$O$_4$ and γ-Fe$_2$O$_3$ films the calculated preferred orientation factor f(311) is 1 and 0.667, respectively. Since the value of f(104) is greater than the other orientation factors in α-Fe$_2$O$_3$ film, therefore it can be said that α-Fe$_2$O$_3$ thin film has preferential orientation along (104) plane. Similarly, for the other films obtained through the conversion i.e. Fe$_3$O$_4$ and γ-Fe$_2$O$_3$ films, the preferred orientation is along (311) plane.

The lattice constants, a and c along with other structural parameter such as strain and dislocation density of the iron oxide films are given in Table 1. The observed values of lattice constants are in agreement with the reported values [21]. Here, the value of lattice constant in γ-Fe$_2$O$_3$ film is smaller than that of Fe$_3$O$_4$ thin films, which is due to the presence of vacancies in γ-Fe$_2$O$_3$.

In thin film configuration, due to textural properties, it is complicated to distinguish the different iron oxide polymorphs; the use of XRD alone cannot assure the presence of a specific phase. For example, Fe$_3$O$_4$ and γ-Fe$_2$O$_3$ showing similar crystal structure cannot be differentiated by XRD. Therefore, for better analysis of iron oxide thin films, other techniques such as Raman spectroscopy and UV–Visible spectroscopy are suggested. We used Raman spectroscopy for the confirmation of iron oxide phase. Figure 2a shows a Raman spectrum of α-Fe$_2$O$_3$ film. Here, no mode is both Raman and infrared active, which is due to an inversion center in hexagonal crystal of α-Fe$_2$O$_3$. The peaks seen at 229 and 499 cm^{-1} are assigned to the A_{1g} mode [28], and peaks at 294, 410 and 609 cm^{-1} are assigned to the E_g mode [28]. All lines typically described for α-Fe$_2$O$_3$ can be identified as: 229 cm^{-1} (A_{1g}), 294 cm^{-1} (E_g), 410 cm^{-1} (E_g), 499 cm^{-1} (A_{1g}) and 609 cm^{-1} (E_g) as indicated in Fig. 2a. The extraneous peak at 662 cm^{-1} in Raman spectra is representative of disorder within the crystal lattice [29, 30]. The line at 1,315 cm^{-1} occurred due to second order scattering process and is specific for the two-phonon or two-magnon scattering process in α-Fe$_2$O$_3$ [31, 32]. Similarly, the Raman spectrum of Fe$_3$O$_4$ thin film is shown in Fig. 2b. This spectrum matches well with reported spectrum in the literature, which shows that there is no feature indicative to either of γ-Fe$_2$O$_3$ and α-Fe$_2$O$_3$ contamination [33]. In this spectrum, the pronounced Fe$_3$O$_4$ feature at 668 cm^{-1} is attributed to A_{1g} mode, whereas the weak features at 315 and 535 cm^{-1} are assigned to T_{1g} mode of vibration [30, 31, 34]. The Raman spectrum of γ-Fe$_2$O$_3$ film is shown in Fig. 2c. We know that the Raman active phonon modes frequency of γ-Fe$_2$O$_3$ is known to vary with preparation method and the distribution of vacancies within the γ-Fe$_2$O$_3$ crystal unit cell [30]. However, the spectra presented in Fig. 2c matches with the reported Raman spectra for γ-Fe$_2$O$_3$ [35], the γ-Fe$_2$O$_3$ film has three observed Raman active phonon modes at 350 cm^{-1} (E_g), 395 (T_{2g}), 507 cm^{-1} (T_{2g}), 670 (A_{1g}) and 708 cm^{-1} (A_{1g}), that exhibit a broad scattering
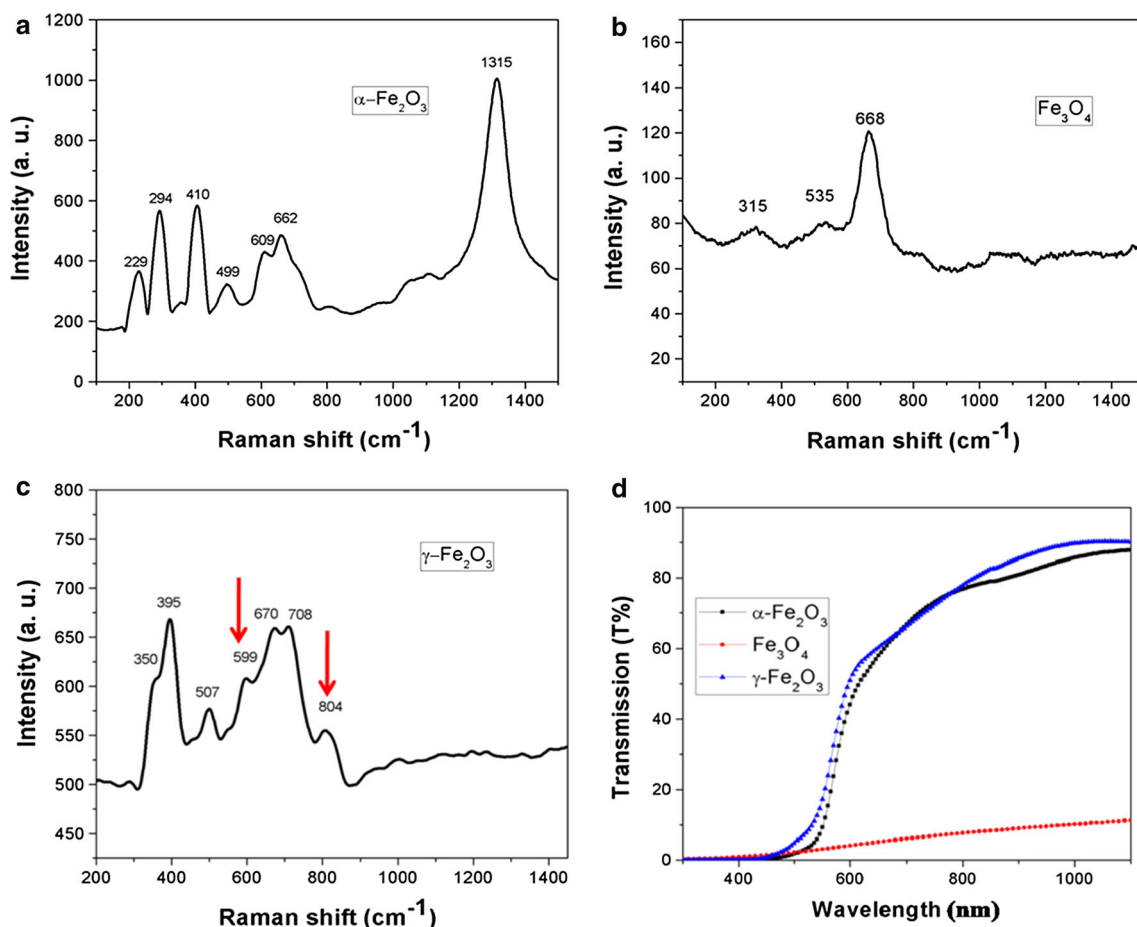
Fig. 2 Raman spectra for, a α-Fe$_2$O$_3$, b Fe$_3$O$_4$, c γ-Fe$_2$O$_3$ films and d is their transmission spectra

response [30, 34, 36]. The additional peaks at 599 and 804 cm^{-1}, as indicated by red arrow, are contributed by the presence of a small amount of α-Fe$_2$O$_3$ phase in the γ-Fe$_2$O$_3$ thin film. The prepared iron oxide thin films are also investigated with the UV–Visible spectroscopy. Figure 2d shows the transmission spectra of iron oxide thin films. Both α-Fe$_2$O$_3$ and γ-Fe$_2$O$_3$ thin films have absorption edge in visible region while no absorption edge is observed in Fe$_3$O$_4$ thin films.

Figure 3 shows the TEM micrographs of the iron oxide thin films. Here, the Fig. 3a is TEM image of α-Fe$_2$O$_3$ thin film and Fig. 3b it its HRTEM image, which indicates lattice spacing equal to 0.2715 nm. The lattice spacing observed from HRTEM is in resemblance with the XRD results. The TEM and HRTEM images of the prepared Fe$_3$O$_4$ thin film are shown in Fig. 3c, d. The Fe$_3$O$_4$ thin film has uniform morphology and lattice spacing value 0.251 nm which corresponds to (311) plane of Fe$_3$O$_4$, this is also similar to the XRD results. Similarly, Fig. 3e, f are TEM and HRTEM images of γ-Fe$_2$O$_3$ film. The lattice spacing in this case have value 0.249 nm which is smaller than the lattice spacing for Fe$_3$O$_4$ which is similar to that of

the XRD result. The inset in Fig. 3a, c, e represents selected area electron diffraction (SAED) patterns of α-Fe$_2$O$_3$, γ-Fe$_2$O$_3$ and Fe$_3$O$_4$ thin films, respectively. The SAEDs show that the films are composed of nanocrystallites. Here, the dotted circles denote crystal planes and the radius of dotted circle is inversely proportional to inter planar spacing. We observed that the crystallite size decreases while going from α-Fe$_2$O$_3$ to Fe$_3$O$_4$ by the reduction in H$_2$ gas, whereas it increases when Fe$_3$O$_4$ film was converted to γ-Fe$_2$O$_3$ be the oxidation in O$_2$ gas. From the TEM images (Fig. 3e) the change in crystallite size can be observed in case of γ-Fe$_2$O$_3$ which is in accordance to the XRD results. From the TEM images, the crystallite size was calculated by using Image J software. The calculated crystallite sizes are 15, 10 and 23 nm for α-Fe$_2$O$_3$, Fe$_3$O$_4$ and γ-Fe$_2$O$_3$ thin films, respectively, which are in close agreement with the XRD results.

For the thickness measurement of the films profilometer was used. The observed thickness of the films is 415, 398 and 408 nm for α-Fe$_2$O$_3$, Fe$_3$O$_4$ and γ-Fe$_2$O$_3$ films, respectively. The observed smaller thickness of the Fe$_3$O$_4$ films as compared with α-Fe$_2$O$_3$ and γ-Fe$_2$O$_3$ films is due

Fig. 3 TEM images **a**, **b** for α-Fe$_2$O$_3$, **c**, **d** for Fe$_3$O$_4$ and **e**, **f** are for Fe$_2$O$_3$ films respectively. The *inset* in **a**, **c** and **e** is the selected area electron diffraction (SAED) of the iron oxide thin films respectively
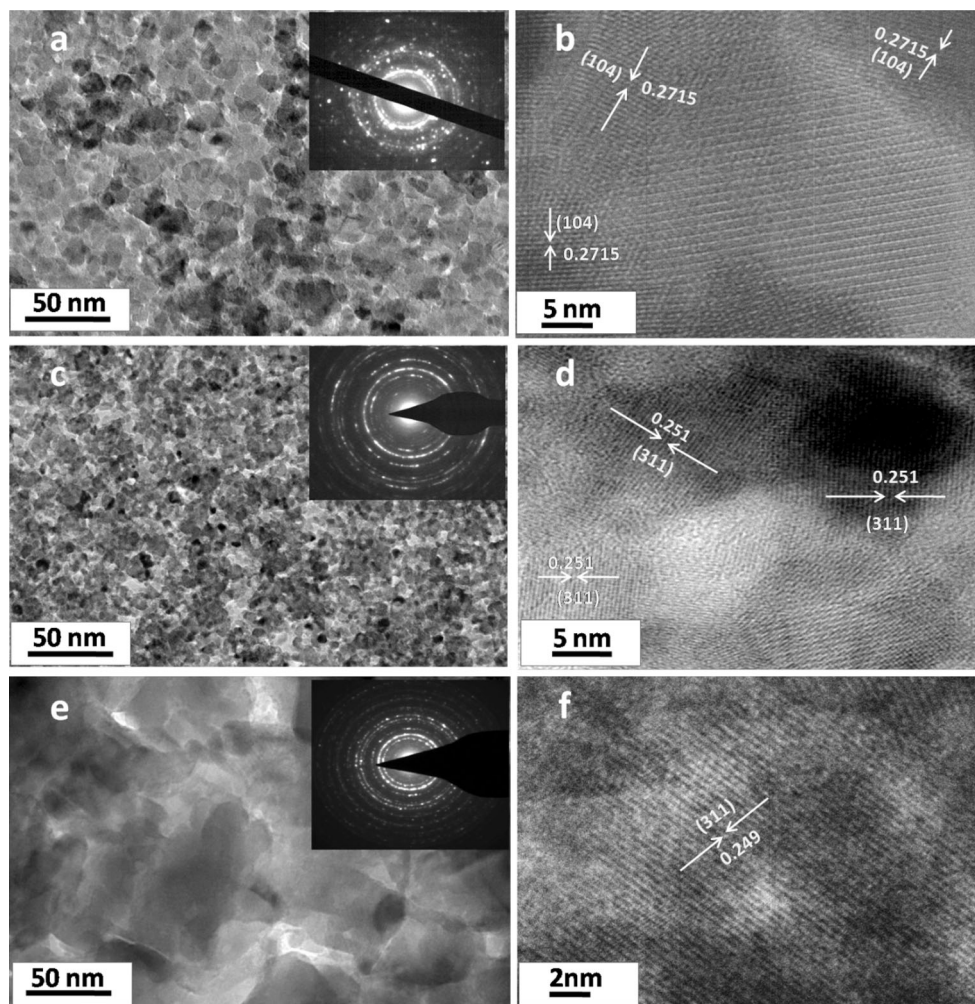
to the magnetite inverse spinel crystal structure that possesses a smaller unit cell than α-Fe$_2$O$_3$ (due to the loss of oxygen) and free of vacancies unlike γ-Fe$_2$O$_3$. To study the surface morphology of the formed iron oxide thin films, AFM was used. The AFM image of α-Fe$_2$O$_3$ film is shown in Fig. 4a, which shows uniform morphology. The average grain size corresponding to the AFM image is about 18 nm as indicated in Fig. 5a. Also, the root means square (*rms*) roughness was measured by AFM image shown in Fig. 4b, which is 4.35 nm. Figure 4c shows the AFM image of Fe$_3$O$_4$ thin film, the corresponding average grain size is 15.4 nm as shown in Fig. 5b, which matches with XRD data. For these Fe$_3$O$_4$ thin films, the *rms* roughness is found 4.602 nm as shown in Fig. 4d, which is close to the roughness value of parent α-Fe$_2$O$_3$ film. This indicates that the roughness of Fe$_3$O$_4$ thin film can be controlled by controlling the roughness of parent α-Fe$_2$O$_3$ film. Therefore, to control the roughness of Fe$_3$O$_4$ film via controlling the roughness of α-Fe$_2$O$_3$ film could be a better way as the α-Fe$_2$O$_3$ film shows negligible magnetic moment in its grain. The decrease in the grain size of the Fe$_3$O$_4$ film is

observed due to the loss of oxygen from α-Fe$_2$O$_3$ grains during reduction process. The AFM image of γ-Fe$_2$O$_3$ thin film is shown in Fig. 4e. Here, the aggregation of particles increases due to the magnetic nature of grain. Also, the annealing process in presence of oxygen increases the particle size due to inter-diffusion of small grains. The average grain size of γ-Fe$_2$O$_3$ thin films is 27 nm as shown in Fig. 5c, which is close to the XRD results. The *rms* roughness in this case is 8.21 nm as shown in Fig. 4f. As mentioned in the proceeding discussion, the increased value of *rms* roughness is due to the aggregation of nanoparticles in the thin film (or large size grains).

3.1 Magnetic properties

Figure 6 shows the room temperature M–H curves of three iron oxide thin films. The corresponding magnetic parameters are given in Table 2. Figure 6a, b shows that the α-Fe$_2$O$_3$ film exhibits super paramagnetic behavior at room temperature. In our previous report [23] we have reported the presence of gamma phase in prepared α-Fe$_2$O$_3$ films, therefore,
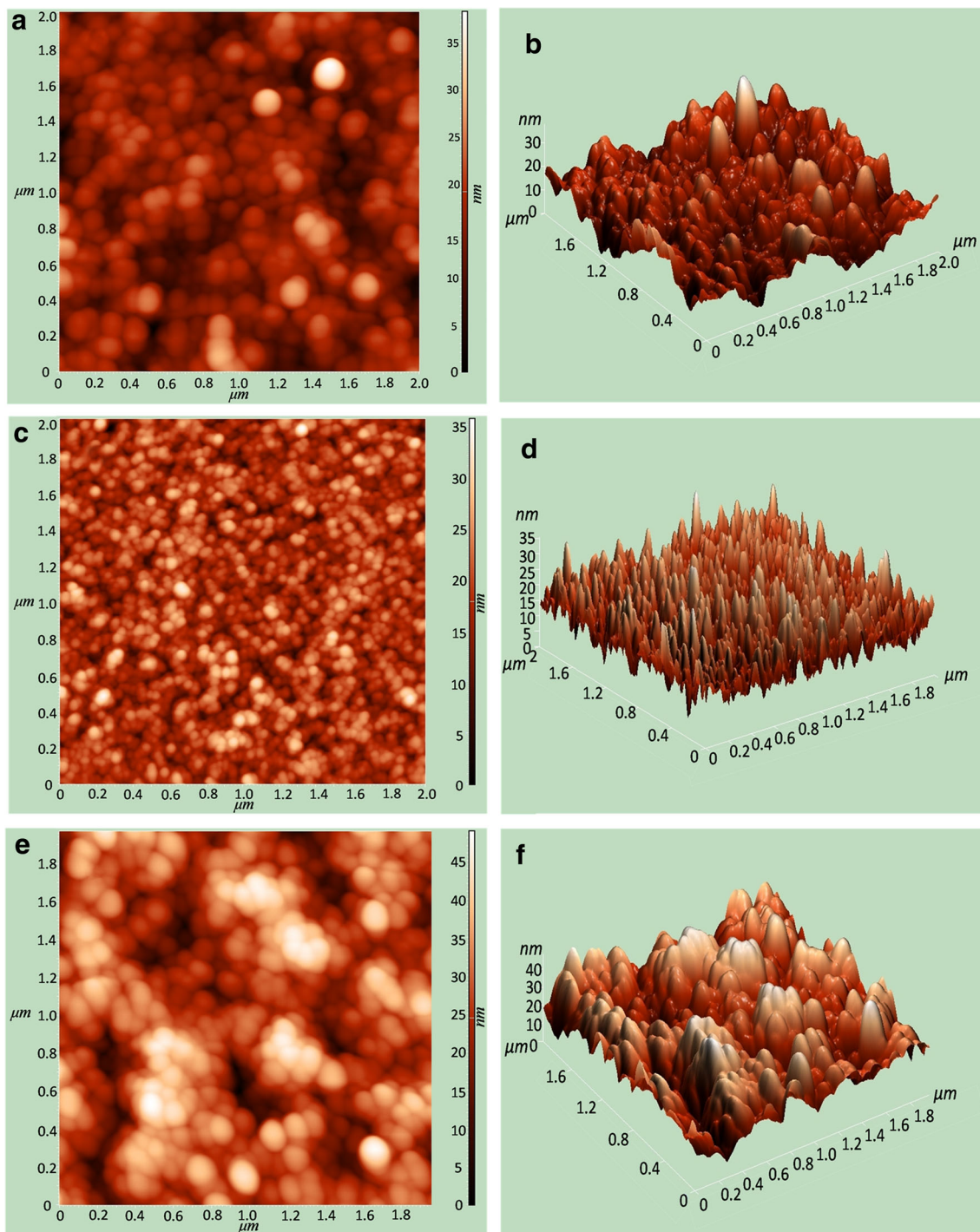
Fig. 4 **a**, **b** 2D and 3D AFM image of the α-Fe$_2$O$_3$ thin film, **c**, **d** is the 2D and 3D AFM image of the Fe$_3$O$_4$ thin film, **e**, **f** are the 2D and 3D AFM image of the γ-Fe$_2$O$_3$ thin film. The entire AFM scan is measurement at 2 × 2 μm scale

to get rid of gamma impurity, the α-Fe$_2$O$_3$ thin films was annealed in O$_2$ environment, which converts all the gamma impurity into α-Fe$_2$O$_3$. The α-Fe$_2$O$_3$ film free of gamma phase was confirmed by XRD and Raman characterizations of the film. The observed value of saturation magnetization of α-Fe$_2$O$_3$ film is 18 emu/cm^3, which is higher than that of its bulk value ($\sim$1 emu/cm^3). The observed higher value of magnetic moment is caused by the uncompensated surface spin canting. We know that the magnetic moment of anti-ferromagnetic nanoparticles (AFNs) is due to the uncompensated surface spins. The magnetic moment contribution by uncompensated surface spins can have any direction with
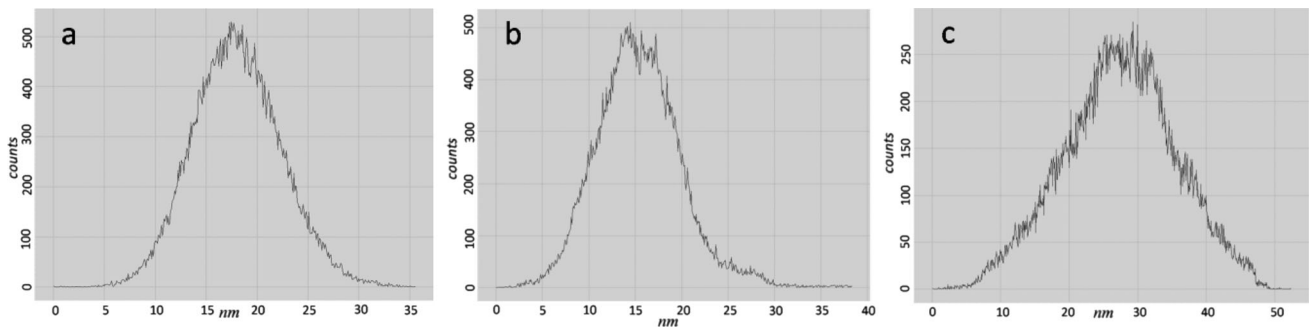
Fig. 5 Grain size distribution as obtained from the AFM data for **a** α-Fe$_2$O$_3$, **b** Fe$_3$O$_4$ and **c** γ-Fe$_2$O$_3$ thin films
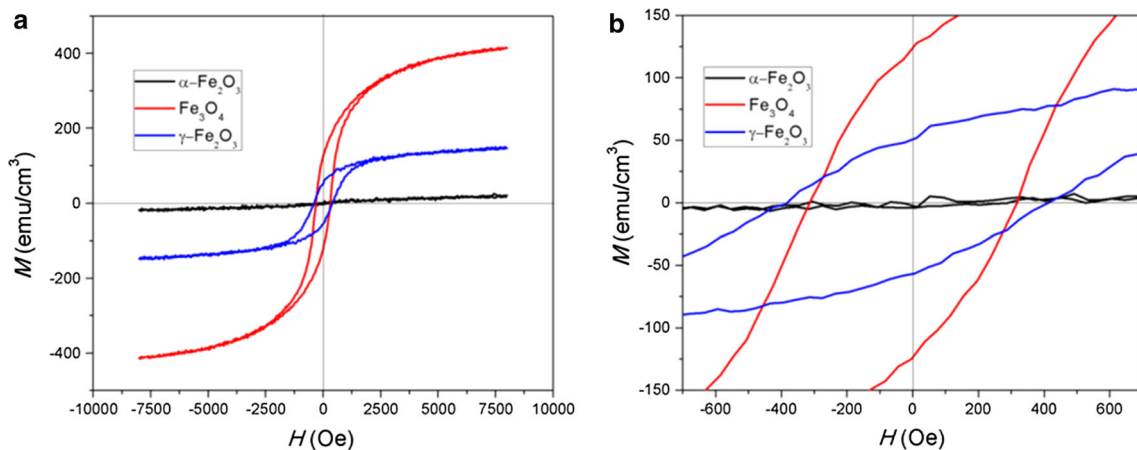
Fig. 6 a M–H plots and **b** enlarged image of the iron oxide thin films at room temperature. The magnetic field is applied in plane during M–H measurement

Table 2 Value of saturation magnetization (M_s), coercivity (H_c) and remanent magnetization (M_r) for iron oxide thin films from VSM result

Sample	M_s (emu/cm^3)	H_c (Oe)	M_r (emu/cm^3)
α-Fe$_2$O$_3$	18	0	0
Fe$_3$O$_4$	414.5	316.5	124.35
γ-Fe$_2$O$_3$	148	400	52

respect to the other magnetic moment contributions. For small values of applied magnetic field, the directions of magnetization of sublattice and the direction of magnetic moment due to uncompensated surface spin are mainly determined by the magnetic anisotropy. For large values of applied magnetic field, the direction of magnetization of sublattice is determined by the competition between the anisotropy energy and Zeeman energy, it also depends upon the relative size of contributions to magnetic moment [37, 38]. In large magnetic fields, the sublattice magnetization directions will approach the applied field direction if the moment due to uncompensated surface spin is greater than the moment due to sublattite magnetization [37, 38]. In case

of nanocrystallites, the contribution due to the uncompensated surface spin is large than the sublattice, hence they show super-paramagnetic behavior. All the uncompensated surface spins get saturated in the direction of external magnetic field, resulting in the super-paramagnetic behavior rather than paramagnetic one. For increased surface spins canting, there is an increase in surface magnetism. Bhowmik et al. [39] has proposed a core–shell model for AFNs where the core is essentially antiferromagnetic and the shell consists of frustrated spins. The situation, where spins of the particle are highly frustrated, is consistent with Neel's prediction of super-paramagnetism in an AFN [39, 40]. The magnetic properties of α-Fe$_2$O$_3$ are reported to varying with the particle size due to the change in lattice symmetry [41].

The Fe$_3$O$_4$ film is found to be ferrimagnetic in nature as indicated in Fig. 6a, b. The observed saturation magnetization (M_s), shown in Table 2, is larger than the reported values [42, 43]. As an example, Lin et al. [22] has reported that the value of M_s and coercivity is 305 emu/cm^3 and 400 Oe, respectively, when the Fe$_3$O$_4$ films of thickness 150 nm was prepared by the reduction of α-Fe$_2$O$_3$. We know that the magnetization of a film decreases with the increasing thickness of Fe$_3$O$_4$ [44]. In our case we observed

that the films are comparatively thicker, therefore, the value of M_s is higher. The observed high value of magnetization indicates less crystallographic defect (antiphase boundaries) and high values of coercivity too, which are due to the crystalline/stress induced anisotropy in Fe_3O_4 thin film [42, 43]. Induced crystalline anisotropy is due to the preferred orientation of Fe_3O_4 films in the [311] direction. Similarly, stress-induced anisotropy arises because of the internal stress which builds up during the growth of the films having thermal expansion coefficient different from that of the substrates. Both the synthesis temperature and preparation method as well affect the density of antiphase boundaries. In an example, the films grown by sputter deposition at 500 °C and molecular beam epitaxy at 225 °C [45] have average size of antiphase domain ranges from 30 to 300 nm, respectively. In our case, as the transition of α-Fe_2O_3 to Fe_3O_4 occurred at 500 °C, the reduced antiphase boundary can be expected.

In case of the γ-Fe_2O_3 thin film, the observed magnetization and coercivity values are 148 emu/cm^3 and 400 Oe, respectively, which are shown in Table 2. These values are smaller than the reported values [46]. Using bulk values of the magnetization such as 1 emu/cm^3 for α-Fe_2O_3 and 430 emu/cm^3 for γ-Fe_2O_3, the concentration of α-Fe_2O_3 phase inside the film is estimated using the formula, $M_s = (x) (M$ of α-$Fe_2O_3) + (1 - x) (M$ of γ-$Fe_2O_3)$, which is found 66 %. In another case, if we consider 18 emu/cm^3 magnetization value of α-Fe_2O_3, the calculated concentration of α-Fe_2O_3 phase is 68 % in the γ-Fe_2O_3 film. Since there is no peak of α-Fe_2O_3 phase in the XRD spectrum and a very small peak in Raman spectrum of γ-Fe_2O_3 film is observed, the decrease in the magnetization value of γ-Fe_2O_3 can be explained in terms of the vacancy of Fe^{3+} ion at octahedral position in γ-Fe_2O_3 structure. From these observations it can be concluded that there is less vacant sites in the sample prepared by the method used in this work. The less number of vacant sites results in small value of saturation magnetization in γ-Fe_2O_3 thin film.

4 Conclusions

The α-Fe_2O_3 thin film has been converted successfully into Fe_3O_4 and γ-Fe_2O_3 thin films by reduction and oxidation process. The pure phase of α-Fe_2O_3 and Fe_3O_4 films have been successfully achieved as confirmed by the Raman spectroscopy. All the three iron oxide thin films have uniform morphology. M–H measurement of the α-Fe_2O_3 film indicates the existence of super-paramagnetism with saturation magnetization value of 18 emu/cm^3, while the Fe_3O_4 and γ-Fe_2O_3 film have been found to be ferrimagnetic in nature. The high value of magnetization in α-Fe_2O_3 thin film is observed due to the uncompensated surface

spins of small α-Fe_2O_3 nanoparticle. The observed lower value of magnetization in case of γ-Fe_2O_3 thin films is due to the less vacancy of the Fe^{3+} ions at the octahedral site in its structure. A higher value of the magnetization in Fe_3O_4 film indicates the efficacy of our process to attain high quality films with less anti-phase boundaries or crystal defects.

References

1. X. He, Y. Zhu, J. Nanosci. Nanotechnol. **12**, 7121 (2012)
2. K. Song, Q. Wang, Q. Liu, H. Zhang, Y. Cheng, Sensors **11**, 485 (2011)
3. H.S. Ryu, J.S. Kim, Z. Guo, H. Liu, K.W. Kim, J.H. Ahn, H.J. Ahn, Phys. Scr. **T139**, 014066 (2010)
4. J.M. Pastor, J.I. Pérez-Landazábal, C. Gómez-Polo, V. Recarte, S. Larumbe, R. Santamarta, M. Fernandes Silva, E.A. Gómez Pineda, A.A. Winkler Hechenleitner, M.K. Lima, Appl. Phys. Lett. **100**, 063102 (2012)
5. R.G. Delatorre, R.C. da Silva, J.S. Cruz, N. Garcia, A.A. Pasa, J. Solid State Electrochem. **13**, 843 (2009)
6. R.N. Goyal, D. Kaur, A.K. Pandey, Mater. Chem. Phys. **116**, 638 (2009)
7. R. Mantovan, A. Lamperti, M. Georgieva, G. Tallarida, M. Fanciulli, J. Phys. D Appl. Phys. **43**, 065002 (2010)
8. S. Shen, C.X. Kronawitter, J. Jiang, S.S. Mao, L. Guo, Nano Res. **5**, 327 (2012)
9. N. Takahashi, N. Kakuda, A. Ueno, K. Yamaguchi, T. Fujii, Jpn. J. Appl. Phys. **28**, L244 (1989)
10. S. Park, S. Lim, H. Choi, Chem. Mater. **18**, 5150 (2006)
11. M.F. Al-Kuhaili, M. Saleem, S.M.A. Durrani, J. Alloys Compd. **521**, 178 (2012)
12. A.P. Caricato, Y.V. Kudryavtsev, G. Leggieri, A. Luches, S.A. Mulenko, J. Phys. D Appl. Phys. **40**, 4866 (2007)
13. B.M. Klahr, A.B.F. Martinson, T.W. Hamann, Langmuir **7**, 461 (2011)
14. H. Yanagihara, M. Myoka, D. Isaka, T. Niizeki, K. Mibu, E. Kita, J. Phys. D Appl. Phys. **46**, 175004 (2013)
15. J.-Y. Lee, B.-C. Kang, D.-Y. Jung, J.-H. Boo, J. Vac. Sci. Technol., B **25**, 1516 (2007)
16. G. Wang, Y. Ling, D.A. Wheeler, K.E.N. George, K. Horsley, C. Heske, J.Z. Zhang, Y. Li, Nano Lett. **11**, 3503 (2011)
17. H.G. Cha, J. Song, H.S. Kim, W. Shin, K.B. Yoon, Y.S. Kang, Chem. Commun. **47**, 2441 (2011)
18. K. Basavaiah, A.V. Prasada Rao, Chem. Sci. Trans. **1**, 1382 (2012)
19. H. Qiu, L. Pan, L. Li, H. Zhu, X. Zhao, M. Xu, L. Qin, J.Q. Xiao, J. Appl. Phys. **102**, 113913 (2007)
20. F. Jiao, J.-C. Jumas, M. Womes, A.V. Chadwick, A. Harrison, P.G. Bruce, J. Am. Chem. Soc. **128**, 12905 (2006)
21. W. Wu, X. Xiao, S. Zhang, J. Zhou, L. Fan, F. Ren, C. Jiang, J. Phys. Chem. C **114**, 16092 (2010)
22. J.K. Lin, J.M. Sivertsen, J.H. Judy, J. Appl. Phys. **57**, 4000 (1985)
23. P. Kumar, R.K. Singh, N. Rawat, P.B. Barman, S.C. Katyal, H. Jang, H.-N. Lee, R. Kumar, J. Nanopart. Res. **15**, 1532 (2013)

24. M. Fang, V. Ström, R.T. Olsson, L. Belova, K.V. Rao, Nanotechnology **23**, 145601 (2012)
25. J.T. Wang, X.L. Shi, W.W. Liu, X.H. Zhong, J.N. Wang, L. Pyrah, K.D. Sanderson, P.M. Ramsey, M. Hirata, K. Tsuri, Sci. Rep. **4**, 3679 (2014)
26. O. Lyandres, D. Finkelstein-Shapiro, P. Chakthranont, M. Graham, K.A. Gray, Chem. Mater. **24**, 3355 (2012)
27. S. Prabahar, M. Dhanam, J. Cryst. Growth **285**, 41 (2005)
28. I. Chamritski, G. Burns, J. Phys. Chem. B **109**, 4965 (2005)
29. D. Bersani, P.P. Lottici, A. Montenero, J. Raman Spectrosc. **30**, 355 (1999)
30. A.M. Jubb, H.C. Allen, ACS Appl. Mater. Interfaces **2**, 2804 (2010)
31. M. Lübbe, A.M. Gigler, R.W. Stark, W. Moritz, Surf. Sci. **604**, 679 (2010)
32. S. Sen, J. Jiang, P. Guo, L. Guo, Int. J. Photoenergy **174982**, 1 (2013)
33. K.W. Chung, K.B. Kim, S.H. Han, H. Lee, J. Electrochem. Soc. **152**, C560 (2005)
34. L. Slavov, M.V. Abrashev, T. Merodiiska, Ch. Geleva, R.E. Vandenberghe, I. Markova-Deneva, I. Nedkov, J. Magn. Magn. Mater. **322**, 1904 (2010)
35. D.L.A. de Faria, S.V. Silva, M.T. de Oliveira, J. Raman Spectrosc. **28**, 873 (1997)
36. M.A. Legodi, D. de Waal, Dyes Pigm. **74**, 161 (2007)
37. F. Bødker, M.F. Hansen, C.B. Koch, K. Lefmann, S. Mørup, Phys. Rev. B **61**, 6826 (2000)
38. R.N. Bhowmik, R. Ranganathan, S. Sarkar, C. Bansal, Mater. Sci. Eng., A **304–306**, 1014 (2001)
39. R.N. Bhowmik, R. Nagarajan, R. Ranganathan, Phys. Rev. B **69**, 054430 (2004)
40. L. Neel, in *Low Temperature Physics*, ed. by C. Dewitt, B. Drefus, P.D. de Gennes (Gordon and Beach, New York, 1962), p. 413
41. L. Lu, L. Li, X. Wang, G. Li, J. Phys. Chem. B **109**, 17151 (2005)
42. A.E. Eken, M. Ozenbas, J. Sol–Gel Sci. Technol. **50**, 321 (2009)
43. Y. Peng, C. Park, D.E. Laughlin, J. Appl. Phys. **93**, 7957 (2003)
44. S.K. Arora, H.-C. Wu, H. Yao, W.Y. Ching, R.J. Choudhary, I.V. Shvets, O.N. Mryasov, IEEE Trans. Magn. **44**, 2628 (2008)
45. W.L. Zhou, K.-Y. Wang, C.J. O'Connor, J. Tang, J. Appl. Phys. **89**, 7398 (2001)
46. O. Ishii, F. Yoshimura, S. Ohara, IEEE Trans. Magn. **MAG-23**, 1985 (1987)